In-situ probing the origin of interfacial instability of Na metal anode

Yuchen Ji,[1,6] Jimin Qiu,[1,6] Wenguang Zhao,[1] Tongchao Liu,[2] Zihang Dong,[3] Kai Yang,[4] Guorui Zheng,[1] Guoyu Qian,[1] Ming Yang,[5] Qindong Chen,[3] Khalil Amine,[2] Feng Pan,[1,*] and Luyi Yang,[1,7,*]

[1] School of Advanced Materials, Peking University Shenzhen Graduate School, Shenzhen, 518055, China.

[2] Chemical Sciences and Engineering Division, Argonne National Laboratory, Argonne, Illinois 60439, USA.

[3] School of Environment and Energy, Peking University Shenzhen Graduate School, Shenzhen, 518055, China.

[4] Advanced Technology Institute, Department of Electrical and Electronic Engineering, University of Surrey, Guildford, Surrey, GU2 7XH, UK.

[5] College of Chemistry and Environmental Engineering, Shenzhen University, Shenzhen 518060, China.

[6] These authors contributed equally.

* Corresponding author. E-mail: panfeng@pkusz.edu.cn (F.P.); yangly@pkusz.edu.cn (L.Y.)

[7] Lead contact. E-mail: yangly@pkusz.edu.cn (L. Y.)

SUMMARY

The unstable and fragile solid–electrolyte interphase (SEI) has restricted the application of Na metal anode. Despite numerous research efforts have been put into understanding its chemical composition and physical property, direct observation of its formation remains a challenge due to the lack of temporal and spatial resolution. Here, through combined *in-situ* probing techniques, we exhibit two pivotal stages associated with SEI instability during the often neglected formation process. It is revealed that Na metal without uniformly passivated at the initial (passivating) stage will trigger unrestricted electrolyte decomposition and homogenous components distribution during the subsequent (growing) stage. SEI with homogenously distributed components is found to have higher solubility than that with a layered structure evolved from a compact passivation layer. Through demonstrating an SEI dissolution model that closely related to its formation process and compositional distribution, this work sheds light on an uncharted territory of Na metal batteries.

INTRODUCTION

Exhibiting high theoretical specific capacity (1165 mAh g^{-1}) and low redox potential (−2.71 V vs standard hydrogen electrode), sodium (Na) metal anode is undeniably the “holy grail” for sodium-ion batteries[1-6]. Unfortunately, the uneven and fragile solid–electrolyte interphase (SEI) cannot endure the enormous volume swing as well as the uncontrolled dendrite growth during repeated Na stripping and plating[7-10]. More importantly, compared with Li-based SEI, Na-based SEI layers tend to dissolve in the electrolyte[11, 12], hence the poor mechanical stability. Consequently, continuous side reactions between Na metal and the electrolyte will eventually cause poor cycling performance and potential safety hazards[13-16].

For better understanding the reaction and dissolution mechanism of instable SEI, scanning electron microscopy (SEM)[8, 17], X-ray photoelectron spectroscopy (XPS)[18-20], secondary ion mass spectroscopy (SIMS)[17], cryogenic transmission electron microscopy (cryo-TEM)[21] and solid state nuclear magnetic resonance (ssNMR)[22, 23] have been employed to acquire interfacial information on Na metal anode by post-mortem analysis. Nevertheless, in order to explore the origin of dissolvability and mechanical instability of SEI buried in the complexed and transient steps of SEI growth, there are still calls for a systematic analyzing approach with both temporal and spatial resolution.

Herein, we harness a wealth of mutually complementary *in-situ* characterization techniques to jointly reveal the SEI instability mechanism and the dynamic picture on SEI evolution at different potentials for Na anode. Integrating macro morphology (*in-situ* 3D laser scanning confocal microscope) and quantitative solubility (electrochemical quartz crystal microbalance) monitoring, we study the SEI instability formed in different electrolytes. Via *in-situ* atomic force microscopy (AFM), we identified two SEI evolution stages (i.e., passivating stage and growing stage). We further find that the absence of effective passivation layer at passivating stage will result in serious electrolyte decomposition and components dissolution in following growing stage by *in-situ* shell-isolated nanoparticle-enhanced Raman spectroscopy (SHINERS). Finally, combined with cryogenic transmission electron microscopy (cryo-TEM) and time-of-flight secondary ion mass spectrometry (TOF-SIMS), we demonstrated that without passivation effect, organic and inorganic components tend to distribute homogenously, which exhibit high dissolvability without enough mechanical support. By contrast, thanks to the pre-formed passivating layer, hierarchical structural SEI with vertically two-layered distribution is formed, which presents higher stability. The method developed in this work combining multiple *in-situ* characterization system can be furtherly expanded to study interfacial evolution in other deposition-type anodes, such as alkali metal anodes[24, 25], aqueous Zn anode[26], etc. In addition, the observed interphase variation also sheds light on how to design robust interfaces in various battery systems.

RESULTS

The stability of SEI

First, the Na deposition behavior in carbonate-based electrolytes (1 M $NaClO_4$ in PC) with and without 5 wt % FEC additive (denoted as PC-FEC and PC, shown in **Figure 1A-J**) was monitored by *in-situ* 3D laser scanning confocal microscope (3D-LSCM). The corresponding 3D contour maps can also be obtained via real-time laser confocal scanning, as presented in **Figure S1, S2**, and the quantitative statistics of roughness variation can also be obtained as showed in **Figure S3** and **Table S1**. In PC-FEC, Na deposition on Cu foil is compact and uniform; whereas a large amount of dendritic, mossy-like and even "dead" Na can be observed during the Na deposition in PC. According to the quantitative analysis (**Figure S3** and **Table S1**), the roughness of pristine Cu foil is around 100 μm and remains nearly unchanged as the deposition of Li in PC-FEC, indicating smooth Na surface due to homogeneous deposition. By sharp contrast, drastic increase of roughness is observed in PC (from ~100 to 170 μm), corresponding to the random Na-deposition and uncontrolled dendrite growth. Such difference in Na deposition behaviors might be attributed to SEIs with higher stability act as an effective protective layer to avoid uneven Na deposition and to Na inhibit dendrite formation[27], drastically enhancing the electrochemical performance in both Na||Cu, Na||Na and full cells (**Figure S4**).

Since Na deposition does not occur until the potential reaching 0 V (vs. Na/Na^+), all electrochemical reactions above 0 V (vs. Na/Na+) can be attributed to the SEI formation and its related side reactions (as shown in **Figure S5**). In the subsequent *in-situ* studies, we will focus on the electrochemical formation process of SEI in a Cu || Na cell by setting the cut-off voltage above 0 V (vs. Na/Na^+). Firstly, electrochemical quartz crystal microbalance (EQCM)[28, 29] was applied to measure the *in-situ* gravimetric variation of SEI formation process (setup shown in **Figure S6**) during galvanostatic reduction processes. As the reduction proceeds, the mass of working electrodes in both electrolytes increases continuously due to the formation of SEI (**Figure 1K and 1L**). When the potential reaches 0 V, the mass accumulation on working electrodes in PC-FEC ($m_{PC\text{-}FEC}$) and PC (m_{PC}) are measured to be 3644 ng and 1030 ng, respectively. To quantitatively evaluate the solubility of SEI, we continue to monitor the mass change during the static stage (i.e. without external current). Both electrodes exhibit instant mass decrease, especially in PC electrolyte, suggesting the continuous dissolution of SEI. Higher dissolution rate is measured in PC (6.5 ng s^{-1} cm^{-2}) compared to in PC-FEC (2.3 ng s^{-1} cm^{-2}), contributing to a less amount of SEI remained on the anode (**Figure S7**). The mass accumulation measured via EQCM is the combined result of both SEI formation and dissolution behaviors. Notably, both mass accumulation (net SEI formation) and decrease (SEI dissolution) are approximately linear with time, indicating a relatively constant SEI formation rate. The gross formation rate of SEI can be obtained via following equation, where v_d is the dissolution rate.

$$\Delta m_{gross} = \int_0^t \nu_d \, dt + \Delta m_{net}$$

The revised mass increase per mole of electron transferred (MPE values) of SEI formation in PC and PC-FEC are 15.4 g mol^{-1} (**Figure S8A and S8C**) and 31.2 g mol^{-1} (**Figure S8B and S8D**), respectively, these values will be later discussed with other *in-situ* results. In addition, the final weights of SEI on two electrodes after equilibrium are measured to be 3353 ng ($m_{PC\text{-}FEC}$') and 463 ng (m_{PC}'), corresponding to dissolution ratios of 8% and 55%, respectively (**Figure 1M**). Therefore, compared with PC, although a higher mass of SEI is formed in PC-FEC, a lower mass is dissolved into the electrolyte. To sum up, the presence of FEC promotes the formation of a heavier SEI with improved stability against dissolution into the electrolyte. Such significant difference in the stability of SEIs raises an intriguing question: what determines the stability of SEI during its transient formation process?

Identifying two stages in SEI formation

In-situ AFM (setup shown in **Figure S9**) driven by linear sweep voltammetry (LSV) was employed for real-time microscopic morphology monitoring the SEI formation on Cu electrode surface in PC (**Figure 2A-2F**) and PC-FEC (**Figure 2I-2N**) from open circuit potential (OCP) to 0 V vs Na/Na$^+$. As presented in **Figure S10**, different electrochemical curves indicate the diverse SEI formation behaviors in both electrolytes.

In PC electrolyte, as the voltage reached ~2.3 V, sparsely distributed particles are observed on the Cu electrode with the size of 100~300 nm (**Figure 2B**). By examining **Figure 2B-2C**, it is clearly shown that the emerge of new particles is accompanied with the disappearance of some previously formed ones (circled in white), which can be attributed to the dissolution into the electrolyte. In comparison, particles formed in PC-FEC electrolyte (~100 nm) are evenly distributed on the surface of Cu electrode (**Figure 2K**) and remain stable (without dissolution) during the scanning process (**Figure 2K-2M**). Thereafter, both electrodes exhibit more distinct SEI formation as the potential reaches around 0.9 V (**Figure 2E and 2M**), which is in accord with the sharp current increase in LSV curves (**Figure S10**). Despite the seemingly similar variation tendency of electrochemical curves, the final morphologies of SEI in PC and PC-FEC are quite different (**Figure 2F and 2N**): the SEI formed in PC-FEC is filled with densely distributed nano-particles. By quantitively measuring the particle sizes *via* cross-sectional analysis, these nano-particles possess highly similar size around 92 nm (**Figure S11**). Contrarily, SEI grows randomly in PC, resulting in relatively loose morphology. The corresponding 3D morphological graphs (**Figure S12**) indicate that in comparison with PC electrolyte, a thicker SEI consists of nano-clusters is formed in PC-FEC, which agrees with the SEI weighting results from EQCM. Based on above morphology evolution, the SEI formation process in both PC and PC-FEC can be roughly divided into Stage I where SEI is initially formed (from ~2.3 V to ~1 V) and Stage II where evident SEI thickening can be observed (from ~1 V to 0 V, marked by dotted line).

Furthermore, the modulus evolution[30] corresponding to the morphology variation in both electrolytes are demonstrated in **Figure S13** and **Figure S14**. The surficial modulus increases homogeneously at around 2.2 V in PC-FEC (**Figure S13C**), in accord with the initial formation potential of Stage I (**Figure 2B**), indicating a solid layer pre-deposited uniformly on Cu. By contrast, the modulus value in PC even decreases lightly at Stage I (**Figure S14B**), which is probably due to the generation of organic electrolyte decomposition products. As the reaction continues, SEI becomes harder in PC-FEC while there is almost no modulus enhancement in PC (**Figure S13E and S14E**). At the end of scanning, the spatial modulus distributions of the SEI surface in PC and PC-FEC are plotted (**Figure 2H and 2P**). The probability distributions of modulus values for SEI formed in PC and PC-FEC (**Figure 2G, 2O and Table S2**) show that SEI modulus in PC-FEC (average 8481.7 Mpa) is an order of magnitude higher than that in PC (average 212.6 Mpa). Such significant difference of rigidity plays a key role for SEI to resist the penetration of Na dendrites, as observed via *in-situ* 3D-LSCM in **Figure 1**.

In-situ probing the formation of passivation layer

To explore the influence of the thin layer formed during Stage I on the stability of SEI, *in-situ* galvanostatic electrochemical impedance spectra (*in-situ* GEIS) were measured by a three-electrode cell (cell configuration and measuring flow as shown in **Figure S15A and S15B**). Since the surface passivation on metal anodes is closely related to the interfacial impedance, *in-situ* GEIS was applied to monitor the impedance variation at different potentials as presented in **Figure 3A and B**. Coincidently, a depressed semicircle can also be detected at Stage I in PC-FEC electrolyte **(Figure 3B)**, which is a characteristic response of interfacial passivation layer. Meanwhile, an additional shoulder peak occurred at relaxation time ~10^{-4} s in the corresponding distribution of relaxation time (DRT) spectrum (**Figure S16**), further verifying the existence of passivation layer. The decreasing tendency of interfacial impedance and peak-shifting to lower relaxation time in DRT results during the subsequent measurements can be attributed to the formation of denser and ionically conductive layer in SEI[31]. By sharp contrast, the interfacial resistance spectrum obtained in PC manifest capacitive response during the whole process, inferring the Cu surface cannot be effectively passivated during Stage I in the absence of FEC (**Figure 3A**). In conclusion, a stable passivation layer with obvious interfacial resistance is formed at early stage of SEI formation in PC-FEC, which do not occur in PC. This result agrees with the *in-situ* AFM measurement, suggesting the robust passivation layer formed in PC-FEC could effectively passivate the anode surface during the SEI formation process.

In-situ shell-isolated nanoparticle-enhanced Raman spectroscopy (*in-situ* SHINERS) was utilized to obtain the interfacial componential information in real-time (**Figure 3C and 3D**). In PC-FEC electrolyte, NaF (**Figure S17A**) can be detected as early as ~2.3 V vs Na/Na^+ (**Figure 3D**), corresponding to the onset of SEI formation (**Figure 2J**). Thus, it is rational to conclude that NaF is one of the main components of the solid layer formed in Stage I (**Figure 2K and Figure S13).** Depth profiling X-ray photoelectron spectroscopy (XPS) was employed to complementally reveal the inner components of this passivation layer (**Figure S18**). The inner composition of SEI formed in PC-FEC shows distinct peak of -CO_3 at 1.3 V (corresponding to Na_2CO_3, **Figure S18K**) along with the signals of Na_2O (**Figure S18I**) and NaF (**Figure S18M**). Thus, the thin and compact layer formed in the initial stage mainly consists of NaF, with small quantities of Na_2O and Na_2CO_3. In comparison, only Na_2O (**Figure S18C**) and a small amount of Na_2CO_3 (**Figure S18B**) are formed as the initial inorganic SEI components in PC at Stage I.

The presence of passivation layer is also found to have further impact on subsequent interfacial reactions during Stage II. On the one hand, as shown in **Figure 3C**, the Raman peak corresponding to NaCl (**Figure S17B**) gradually weakens in PC, whereas Raman signals of NaF and NaCl in PC-FEC (**Figure 3D**) are continuously growing. Considering the low solubility of NaCl in electrolyte, we speculate that compared with NaCl formed in PC-FEC that can stably exist in the SEI, NaCl formed in PC cannot be retained due to the possible detachment. On the other hand, the Raman peaks for the ingredient of electrolyte (PC and $NaClO_4$, **Figure S17C**) gradually vanished in PC as the voltage decreased, indicating the consumption of electrolyte without passivated surface, which leads to the low coulombic efficiency.

Moreover, to reveal the SEI formation mechanism, *in-situ* differential electrochemical mass spectrometry (DEMS) was applied for gas detection during the SEI formation process (**Figure 3E and 3F**). As expected, the gas evolution process also demonstrates distinct two stages, which can be roughly marked off by the potential around 1 V vs Na/Na^+. First, both PC and PC-FEC release C_3H_6 from ~2.3 to ~1 V. According to the XPS analysis, the Na_2CO_3 and Na_2O are also formed within this potential range. We speculate that Na_2CO_3 and Na_2O are generated from the electrochemical decomposition reaction between PC and Na^+ as presented in **Equation 1 – 3**.

(1)

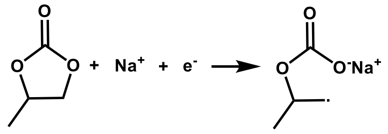

(2)

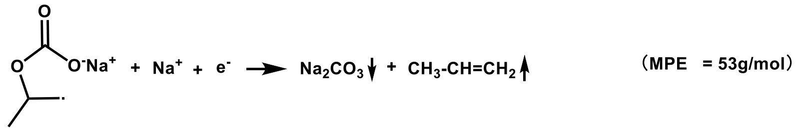

(3)

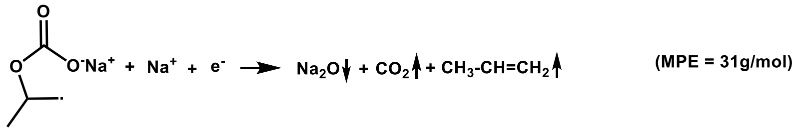

Due to the presence of FEC additive, additional FEC-related reactions (**Equation 4-6**) occur in PC-FEC, resulting in the characteristic C_2H_3F release in both stages. Consequently, extra formation paths are facilitated for inorganic Na_2CO_3 and Na_2O.

(4)

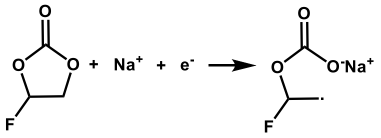

(5)

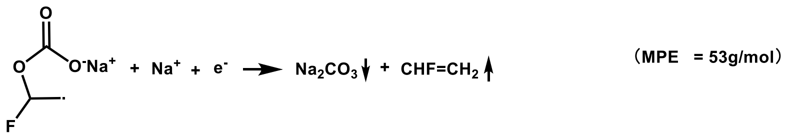

(6)

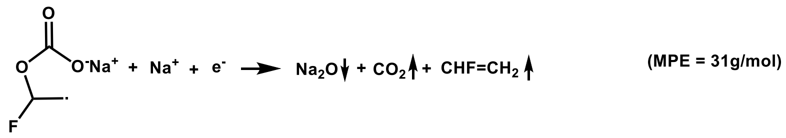

Furthermore, due to the unsaturated carbon-carbon bonds in C_3H_6 and C_2H_3F, both of them can be further polymerized into polyacetylene releasing H_2 as shown in **Equation 7** and **Equation 8**. The inhibited H_2 release in PC-FEC (**Figure 3F**) indicates a well-passivated electrode surface that retards the polymerization reactions. In addition, extra NaF can be formed in PC-FEC during the polymerization of C_2H_3F.

(7) 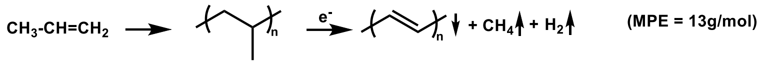

(8) 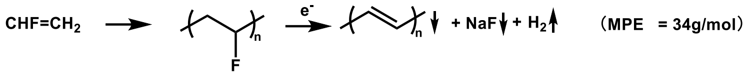

CO_2 is also detected accompanied by CH_4 in both electrolytes. We speculate the possible reactions are due to the direct electrochemical reduction of PC (**Equation 9**), which may trigger the formation dissolvable organic products as presented in **Equation 10**.[32] In comparison, the direct reduction of FEC generates NaF as presented in **Equation 11**, which boosts the chemical and mechanical stability of SEI simultaneously.

(9) 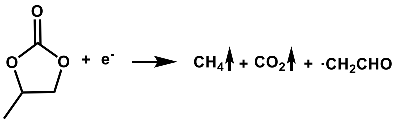

(10) 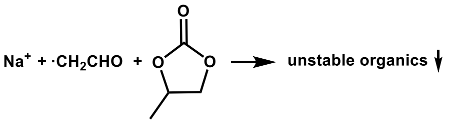

(11) 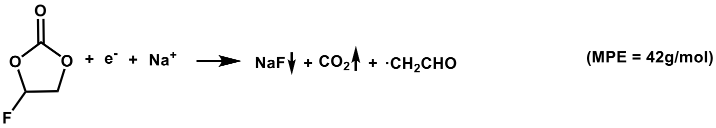

The speculative reaction of NaCl decomposed from $NaClO_4$ in both two electrolytes is presented in **Equation 12**, which also subsequently causes the generation of Na_2O and various organic products presented in **Equation 13**.[32]

(12) $NaClO_4 + e^- \rightarrow NaCl\downarrow + O^{2-}$ (MPE = 7.3g/mol)

(13) 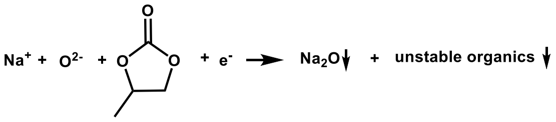

According to the gravimetric results of EQCM, the revised average MPE value of SEI formation in PC and PC-FEC are 15.4 g mol^{-1} and 31.2 g mol^{-1} (**Figure S8**), respectively. By comparing these values with the theoretical MPE values of above reactions, it can be concluded that in PC, SEI mainly consists of electrolyte reduction products with low MPE values e.g. polypropylene (13 g mol^{-1}), whereas inorganic products with relatively high MPE values such as Na_2CO_3 (53 g mol^{-1}) and Na_2O (31 g mol^{-1}) are minor components. By contrast, the higher MPE value obtained in PC-FEC infers that the SEI is predominantly composed of NaF (42 g mol^{-1} *via* FEC reduction and 34 g mol^{-1} *via* C_2H_3F polymerization), Na_2CO_3 (53 g mol^{-1}) and Na_2O (31 g mol^{-1}). Therefore, the presence of FEC provides alternative reaction routes that form SEI components with more desirable properties with equimolar quantities of electrons transferred, resulting in radically different SEI properties.

Detecting spatial distribution of SEI components

So far, vastly different SEI formation process and corresponding reaction routes have been observed in two electrolytes. To unveil their impact on the stability of SEI, the micro-structure of SEI is observed via cryogenic transmission electron microscopy (cryo-TEM) (**Figure 4A and 4B**). SEI formed in PC is discontinuous with exposed Na surface due to its tendency to dissolve in the electrolyte. In comparison, PC-FEC electrolyte results in a thicker SEI that fully covers the Na anode. Coincidentally, semicircular particles with diameters around 92.5 nm are found to embed in the SEI layer formed in PC-FEC, which agrees with the particle size (~92 nm) measured by *in-situ* AFM **(Figure S11)**. Energy dispersive spectroscopy (EDS) (**Figure 4C and 4D**), confirms that these island-like particles are NaF. On the contrary, no distinct particles can be observed in the SEI formed in PC **(Figure 4A and S19)**.

Due to the measuring limitations of *in-situ* SHINERS (e.g. selective signal enhancement and limited detection depth), we further applied TOF-SIMS to probe in-depth information of SEI to reconstruct its inner componential distribution via 3D-vislizaiton and quantitative analysis. The signal of Na_2CO_3, Na_2O, NaCl and organic component (identified with $-CH^-$) are clearly detected in both PC (**Figure 4E**) and PC-FEC (**Figure 4F**), and the normalized intensities of these fragments are also compared (**Figure 4G, 4H and S20**). For the SEI formed in PC**,** the distribution of inorganic is spatially mixed with organic component (**Figure 4E)**. According to the quantitative comparison (**Figure 4G**), organic species exist extensively throughout the SEI, whereas inorganic components including Na_2CO_3, Na_2O and NaCl co-exist with organic species, showing very little variation in vertical distribution. Based on this structure, one could speculate that in PC, once organic components are dissolved away, the adjacent inorganic particles will be detached from the SEI. Contrarily, in PC-FEC (**Figure 4H)**, the organic components are dominant in a 10 nm layer at the top of SEI, and the bottom part predominantly consists of inorganics, and the intensity of Na_2CO_3 even surpasses $-CH^-$ at ~40 nm. Combining these quantitative results to the 3D-graph of PC-FEC (**Figure 4F**), a hierarchical structure with vertically two-layered distribution is built within the SEI, where abundant inorganic components are located at the bottom of SEI and organics mainly cover on the top. In this case, the dissolve of organic species will have little effect on the inorganics.

In addition, *in-situ* laser particle size measurement was applied to monitor the detachment of SEI particles into the electrolyte (**Figure S21**). The signal of particle increases significantly in PC at Stage II, indicating that some insoluble particles detached away from SEI in PC. Combining this phenomenon with EQCM results, it can be speculated that the mass loss is contributed by not only the dissolution of organics, but also the detachment of insoluble species.

DISCUSSION

Combining all results together, the origin of SEI chemical and mechanical instability can be revealed through a dissolution model (**Scheme 1). ** At Stage I (from ~2.3 V to ~1 V vs Na/Na$^+$), soluble polymers/oligomers are the main SEI composition, which fail to passivate and lead to the exposed Na anodes to the electrolyte (**Scheme 1A**). When the potential reaches below 1 V, both organics and inorganics formed directly on the Na surface, however, due to the high solubility, organics are formed and dissolved repeatedly on Na metal, leaving the inorganic components detached from the electrode. Consequently, inorganic components are randomly embedded in organic components with low modulus (**Scheme 1B**), which tend to be dissolved away from the SEI as they lost contact with the binding polymeric species during the repeated generating-dissolving process, leading to poor stability of the SEI. (**Scheme 1C**)

The stability of SEI can be efficiently enhanced via pre-constructing an inorganic passivation layer on the surface of Na at Stage I, which minimizes the contact area between electrolyte and Na metal (**Scheme 1D**). Subsequently, the inorganic species gradually grow into a thicker and harder passivating layer that being attached tightly on the surface of Na metal, while organic decomposition products can only grow on the top of this passivation layer (**Scheme 1E**). Such hierarchical structure provides good protection of Na metal surface and high modulus to resist the dendrite growth (**Scheme 1F**).

The dynamic analysis of SEI evolution of Na anode presented in this work sheds light on how to construct a stable SEI, and similar strategies can also be widely applied to study the interfacial evolution of other electrolyte system, such as alternative Na salt ($NaPF_6$, NaFSI, etc.) or solvents (EC, DME, etc.). In addition, the developed methodology combining multiple *in-situ* characterizations in this work (**Table S3**) can be furtherly expanded to study other depositional anodes, such as alkali metal anodes, aqueous Zn anodes, etc., providing guiding significance in unveiling the seemingly complicated interfacial chemistry in batteries via a concerted characterization approach.

EXPERIMENTAL PROCEDURES

Resource Availability

Lead Contact

Further information and requests for resources should be directed to and will be fulfilled by the lead contact, Luyi Yang (yangly@pkusz.edu.cn).

Materials Availability

This study did not generate new unique reagents.

Data and Code Availability

Any additional information required to reanalyze the data reported in this paper is available from the lead contact upon request. Full experimental procedures are described in the supplemental information.

SUPPLEMENTAL INFORMATION

Supplemental Information can be found online at https://doi.org/... …

ACKNOWLEDGEMENTS

This work was supported by The Shenzhen Science and Technology Research Grant (JCYJ20200109140416788) and the Soft Science Research Project of Guangdong Province (2017B030301013). The authors would like to thank Shiyanjia Lab for TOF-SIMS analysis.

AUTHOR CONTRIBUTIONS

Conceptualization, Y.J., Q.J. and L.Y.; Methodology, Y.J. and Q.J.; Investigation, Y.J., Q.J., W.Z., T.L., Z.D., K.Y., G.Z., G.Q., M.Y. and Q.C.; Resources, K.A., F.P. and L.Y.; Writing – Original Draft, Y.J. and J.Q.; Writing – Review & Editing, F.P. and L.Y.; Supervision, F.P. and L.Y.; Project Administration, L.Y.; Funding Acquisition, F.P. and L.Y.

DECLARATION OF INTERESTS

The authors declare no competing interests.

REFERENCES

1. Xiang, J., Yang, L., Yuan, L., Yuan, K., Zhang, Y., Huang, Y., Lin, J., Pan, F., and Huang, Y. (2019). Alkali-Metal Anodes: From Lab to Market. Joule *3*, 2334-2363. https://doi.org/10.1016/j.joule.2019.07.027.
2. Yabuuchi, N., Kubota, K., Dahbi, M., and Komaba, S. (2014). Research development on sodium-ion batteries. Chem. Rev. *114*, 11636-11682. https://doi.org/10.1021/cr500192f.
3. Palomares, V., Serras, P., Villaluenga, I., Hueso, K.B., Carretero-González, J., and Rojo, T. (2012). Na-ion batteries, recent advances and present challenges to become low cost energy storage systems. Energ. Environ. Sci. *5*. https://doi.org/10.1039/c2ee02781j.
4. Zhao, Y., Adair, K.R., and Sun, X. (2018). Recent developments and insights into the understanding of Na metal anodes for Na-metal batteries. Energ. Environ. Sci. *11*, 2673-2695. https://doi.org/10.1039/c8ee01373j.
5. Liu, H., Cheng, X.-B., Jin, Z., Zhang, R., Wang, G., Chen, L.-Q., Liu, Q.-B., Huang, J.-Q., and Zhang, Q. (2019). Recent advances in understanding dendrite growth on alkali metal anodes. EnergyChem *1*, 100003. https://doi.org/10.1016/j.enchem.2019.100003.

6. Bao, C., Wang, B., Liu, P., Wu, H., Zhou, Y., Wang, D., Liu, H., and Dou, S. (2020). Solid Electrolyte Interphases on Sodium Metal Anodes. Adv. Funct. Mater. *30*, 2004891. https://doi.org/10.1002/adfm.202004891.
7. Lee, J., Kim, J., Kim, S., Jo, C., and Lee, J. (2020). A review on recent approaches for designing the SEI layer on sodium metal anodes. Materials Advances *1*, 3143-3166. https://doi.org/10.1039/d0ma00695e.
8. Hu, J., Wang, H., Wang, S., Lei, Y., Qin, L., Li, X., Zhai, D., Li, B., and Kang, F. (2021). Electrochemical deposition mechanism of sodium and potassium. Energy Storage Mater.*36*, 91-98. https://doi.org/10.1016/j.ensm.2020.12.017.
9. Eshetu, G.G., Elia, G.A., Armand, M., Forsyth, M., Komaba, S., Rojo, T., and Passerini, S. (2020). Electrolytes and Interphases in Sodium-Based Rechargeable Batteries: Recent Advances and Perspectives. Adv. Energy Mater. *10*. https://doi.org/10.1002/aenm.202000093.
10. Bao, C., Wang, B., Liu, P., Wu, H., Zhou, Y., Wang, D., Liu, H., and Dou, S. (2020). Solid Electrolyte Interphases on Sodium Metal Anodes. Adv. Funct. Mater. *30*. https://doi.org/10.1002/adfm.202004891.
11. Mogensen, R., Brandell, D., and Younesi, R. (2016). Solubility of the Solid Electrolyte Interphase (SEI) in Sodium Ion Batteries. ACS Energy Lett. *1*, 1173-1178. https://doi.org/10.1021/acsenergylett.6b00491.
12. Ahsan, Z., Ding, B., Cai, Z., Wen, C., Yang, W., Ma, Y., Zhang, S., Song, G., and Javed, M.S. (2021). Recent progress in capacity enhancement of $LiFePO_4$ cathode for Li-Ion batteries. J. Electrochem. Energy *18*. https://doi.org/10.1115/1.4047222.
13. Kim, S.-W., Seo, D.-H., Ma, X., Ceder, G., and Kang, K. (2012). Electrode Materials for Rechargeable Sodium-Ion Batteries: Potential Alternatives to Current Lithium-Ion Batteries. Adv. Energy Mater. *2*, 710-721. https://doi.org/10.1002/aenm.201200026.
14. Zhang, C., Wang, A., Zhang, J., Guan, X., Tang, W., and Luo, J. (2018). 2D Materials for Lithium/Sodium Metal Anodes. Adv. Energy Mater. *8*. https://doi.org/10.1002/aenm.201802833.
15. Zhao, C., Lu, Y., Yue, J., Pan, D., Qi, Y., Hu, Y.-S., and Chen, L. (2018). Advanced Na metal anodes. J. Energy Chem. *27*, 1584-1596. https://doi.org/10.1016/j.jechem.2018.03.004.
16. Liu, T., Yang, X., Nai, J., Wang, Y., Liu, Y., Liu, C., and Tao, X. (2021). Recent development of Na metal anodes: Interphase engineering chemistries determine the electrochemical performance. Chem. Eng. J. *409*. https://doi.org/10.1016/j.cej.2020.127943.
17. Dahbi, M., Yabuuchi, N., Fukunishi, M., Kubota, K., Chihara, K., Tokiwa, K., Yu, X.-f., Ushiyama, H., Yamashita, K., Son, J.-Y., Cui, Y.-T., Oji, H., and Komaba, S. (2016). Black Phosphorus as a High-Capacity, High-Capability Negative Electrode for Sodium-Ion Batteries: Investigation of the Electrode/Electrolyte Interface. Chem. Mater. *28*, 1625-1635. https://doi.org/10.1021/acs.chemmater.5b03524.
18. Mogensen, R., Maibach, J., Brant, W.R., Brandell, D., and Younesi, R. (2017). Evolution of the solid electrolyte interphase on tin phosphide anodes in sodium ion batteries probed by hard x-ray photoelectron spectroscopy. Electrochim. Acta *245*, 696-704. https://doi.org/10.1016/j.electacta.2017.05.173.

19. Pan, K., Lu, H., Zhong, F., Ai, X., Yang, H., and Cao, Y. (2018). Understanding the Electrochemical Compatibility and Reaction Mechanism on Na Metal and Hard Carbon Anodes of PC-Based Electrolytes for Sodium-Ion Batteries. ACS Appl. Mater. Interfaces *10,* 39651-39660. https://doi.org/10.1021/acsami.8b13236.
20. Gimble, N.J., Kraynak, L.A., Schneider, J.D., Schulze, M.C., and Prieto, A.L. (2021). X-ray photoelectron spectroscopy as a probe for understanding the potential-dependent impact of fluoroethylene carbonate on the solid electrolyte interface formation in Na/Cu2Sb batteries. J. Power Sources *489*. https://doi.org/10.1016/j.jpowsour.2020.229171.
21. Han, B., Zou, Y., Zhang, Z., Yang, X., Shi, X., Meng, H., Wang, H., Xu, K., Deng, Y., and Gu, M. (2021). Probing the Na metal solid electrolyte interphase via cryo-transmission electron microscopy. Nat. Commun. *12,* 3066. https://doi.org/10.1038/s41467-021-23368-6.
22. Gao, L.N., Chen, J.E., Chen, Q.L., and Kong, X.Q. (2022). The chemical evolution of solid electrolyte interface in sodium metal batteries. Sci. Adv. *8*. https://doi.org/ARTN eabm4606
23. Xiang, Y., Zheng, G., Liang, Z., Jin, Y., Liu, X., Chen, S., Zhou, K., Zhu, J., Lin, M., He, H., Wan, J., Yu, S., Zhong, G., Fu, R., Li, Y., and Yang, Y. (2020). Visualizing the growth process of sodium microstructures in sodium batteries by in-situ (23)Na MRI and NMR spectroscopy. Nat. Nanotechnol. *15,* 883-890. https://doi.org/10.1038/s41565-020-0749-7.
24. Qian, S., Chen, H., Zheng, M., Zhu, Y., Xing, C., Tian, Y., Yang, P., Wu, Z., and Zhang, S. (2023). Complementary combination of lithium protection strategies for robust and longevous lithium metal batteries. Energy Storage Mater.*57,* 229-248. https://doi.org/10.1016/j.ensm.2023.02.019.
25. Qian, S., Xing, C., Zheng, M., Su, Z., Chen, H., Wu, Z., Lai, C., and Zhang, S. (2022). CuCl2-Modified Lithium Metal Anode via Dynamic Protection Mechanisms for Dendrite-Free Long-Life Charging/Discharge Processes. Adv. Energy Mater. *12,* 2103480. https://doi.org/10.1002/aenm.202103480.
26. Doose, S., Mayer, J.K., Michalowski, P., and Kwade, A. (2021). Challenges in ecofriendly battery recycling and closed material cycles: a perspective on future lithium battery generations. Metals *11*, 291. https://doi.org/10.3390/met11020291.
27. Han, M., Zhu, C., Ma, T., Pan, Z., Tao, Z., and Chen, J. (2018). In situ atomic force microscopy study of nano-micro sodium deposition in ester-based electrolytes. Chem. Commun. (Camb) *54*, 2381-2384. https://doi.org/10.1039/c7cc09751d.
28. Ji, Y., Yin, Z.W., Yang, Z., Deng, Y.P., Chen, H., Lin, C., Yang, L., Yang, K., Zhang, M., Xiao, Q., Li, J.T., Chen, Z., Sun, S.G., and Pan, F. (2021). From bulk to interface: electrochemical phenomena and mechanism studies in batteries via electrochemical quartz crystal microbalance. Chem. Soc. Rev. *50,* 10743-10763. https://doi.org/10.1039/d1cs00629k.
29. Qin, R., Wang, Y., Zhao, Q., Yang, K., and Pan, F. (2020). EQCM for In-depth Study of Metal Anodes for Electrochemical Energy Storage. Chinese J. Struct. Chem. *39,* 605-614. https://doi.org/10.14102/j.cnki.0254-5861.2011-2819
30. Jia, L., Ji, Y., Yang, K., Wang, Z., Chen, H., and Pan, F. (2020). Interface Reconstruction Study by Functional Scanning Probe Microscope in Li-ion Battery Research. Chinese J. Struct. Chem. *39*, 200─205. https://doi.org/10.14102/j.cnki.0254-5861.2011-2749.

31. Lu, Y., Zhao, C.-Z., Huang, J.-Q., and Zhang, Q. (2022). The timescale identification decoupling complicated kinetic processes in lithium batteries. Joule *6*, 1172-1198. https://doi.org/10.1016/j.joule.2022.05.005.
32. Aurbach, D., Markevich, E., and Salitra, G. (2021). High Energy Density Rechargeable Batteries Based on Li Metal Anodes. The Role of Unique Surface Chemistry Developed in Solutions Containing Fluorinated Organic Co-solvents. J. Am. Chem. Soc. *143*, 21161-21176. https://doi.org/10.1021/jacs.1c11315.

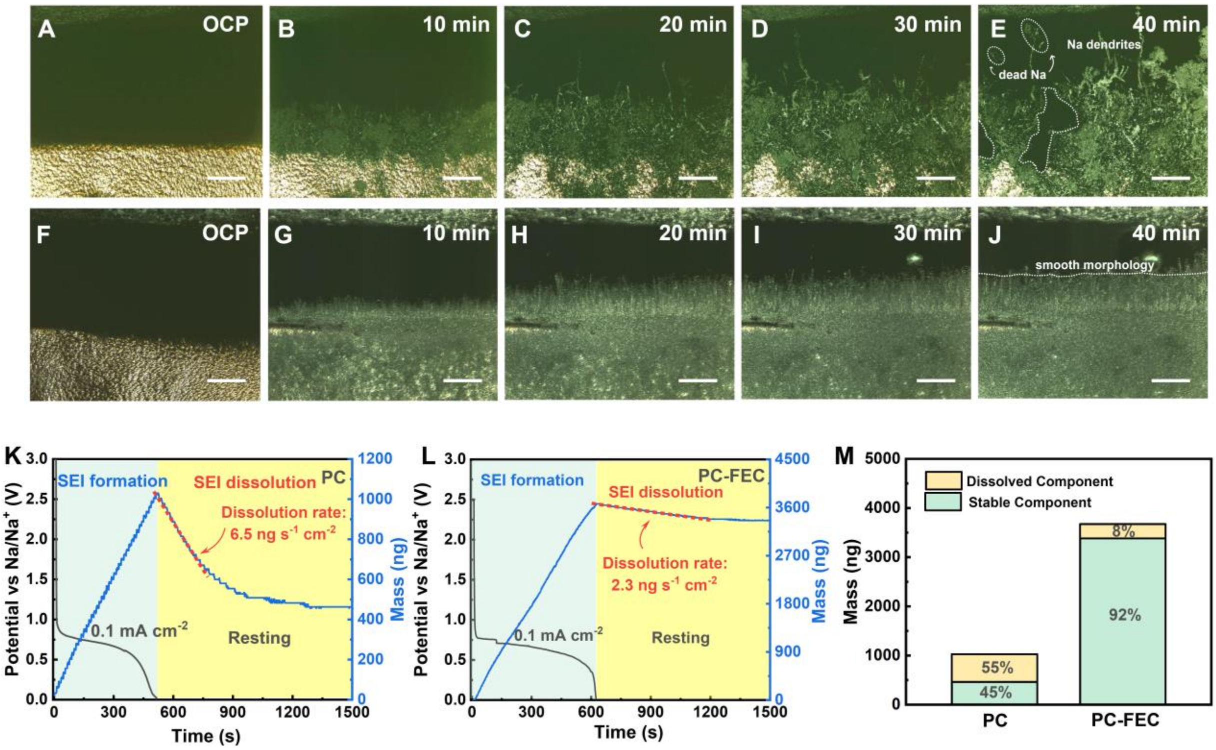

Figure 1. The stability of SEI in PC and PC-FEC

(A-J) *In-situ* 3D-LSCM observation of the Na deposition morphologies in PC (A-E) and PC-FEC (F-J) at 1 mA cm^{-2}. (Scale bar: 100 μm).

(K and L) *In-situ* EQCM weighing results of mass variations in PC (K) and PC-FEC (L) at the discharging rate of 0.1 mA cm^{-2}.

(M) Total mass and mass ratios of dissolved and stable components in the SEI formed at 0 V in different electrolytes.

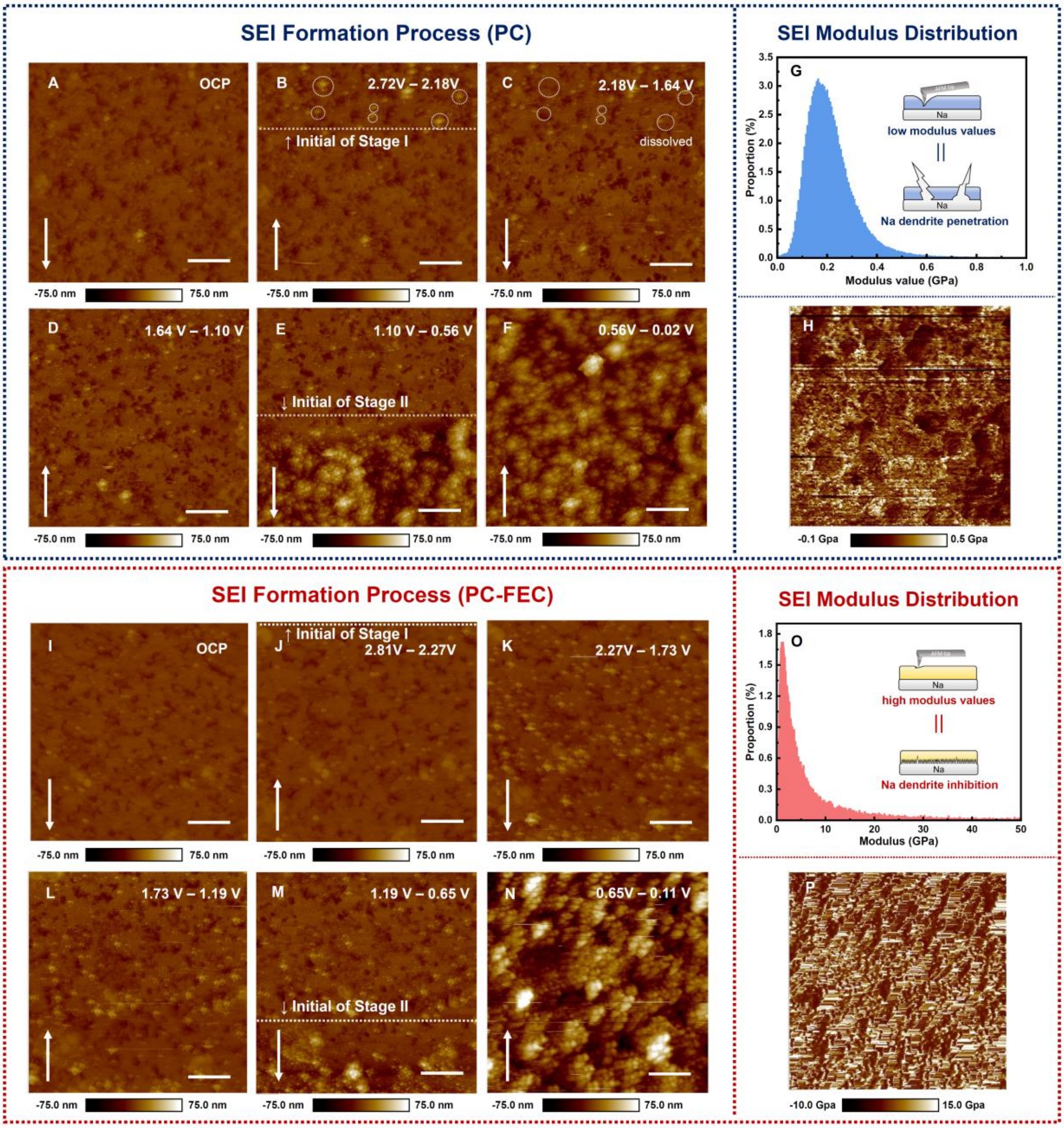

Figure 2. ***In-situ* morphological and mechanical detection of SEI formation process via *in-situ* AFM**

(A-F) *In-situ* AFM detecting SEI morphological evolution on Cu current collector in PC.

(G) Probability distribution of PC formed SEI modulus values.

(H) Spatial distribution of PC formed SEI modulus values.

(I-N) *In-situ* AFM detecting SEI morphological evolution on Cu current collector in PC-FEC.

(O) Probability distribution of PC-FEC formed SEI modulus values.

(P) Spatial distribution of PC-FEC formed SEI modulus values. (Scale bar: 1 μm).

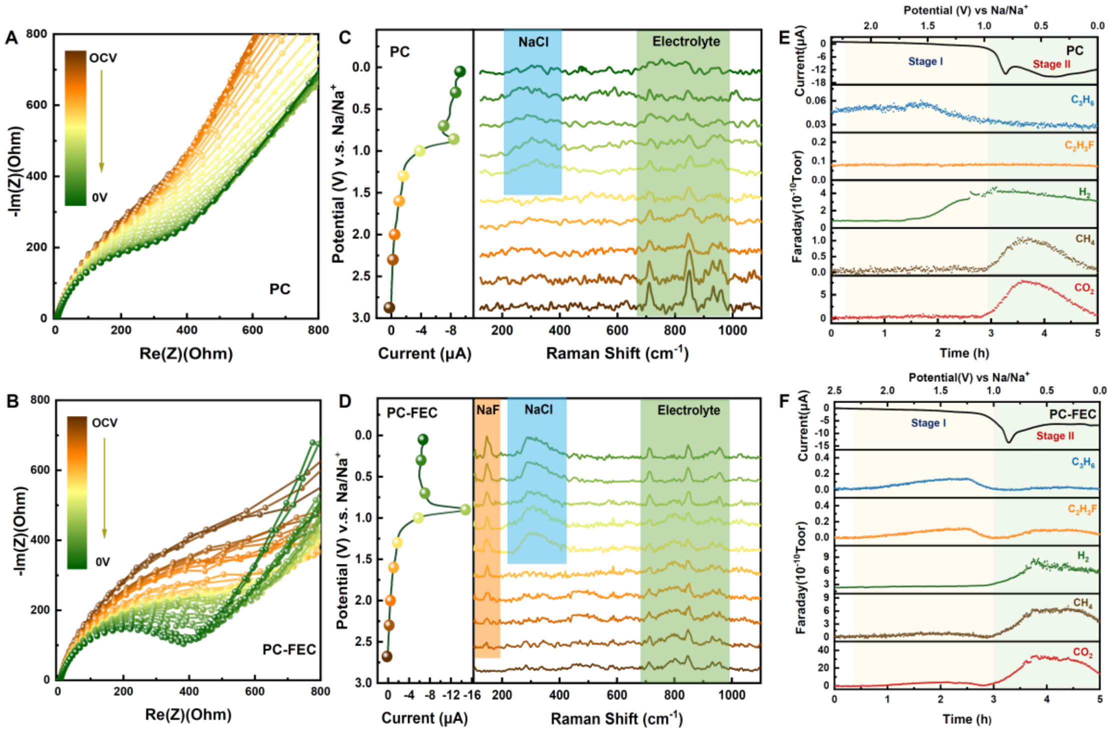

Figure 3. *In-situ* detecting the formation of passivation layer and the subsequent evolution

(A and B) *In-situ* GEIS result of corresponding potentials during the two stages in PC (A) and PC-FEC (B).

(C and D) *In-situ* SHINERS result of SEI formation in PC (C) and PC-FEC (D).

(E and F) LSV curves and corresponding gaseous release detection measured via DEMS during SEI formation in PC (E) and PC-FEC (F).

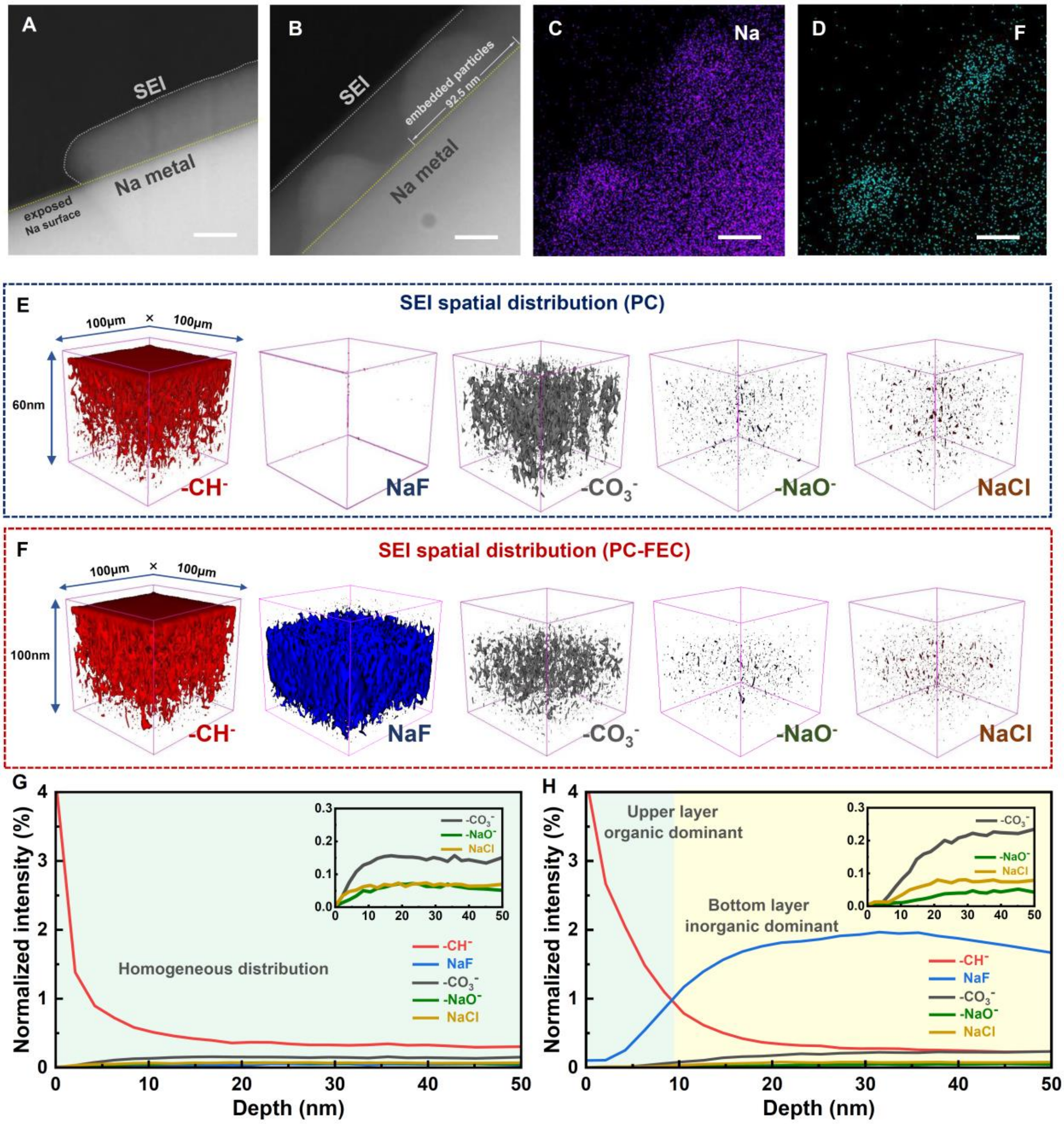

Figure 4. Inner spatial distribution of SEI components

(A and B) Cryo-TEM graph of formed SEI morphology in PC (A) and PC-FEC (B) (Scale bar: 30 nm).

(C and D) Corresponding elemental analysis via TEM- EDS of SEI in PC-FEC.

(E and F) 3D distribution of various components inner SEI measured via TOF-SIMS in PC (E) and PC-FEC (F).

(G and H) The normalized TOF-SIMS signal intensities of various components at depth of above 50nm of the SEI formed in PC (G) and PC-FEC (H).

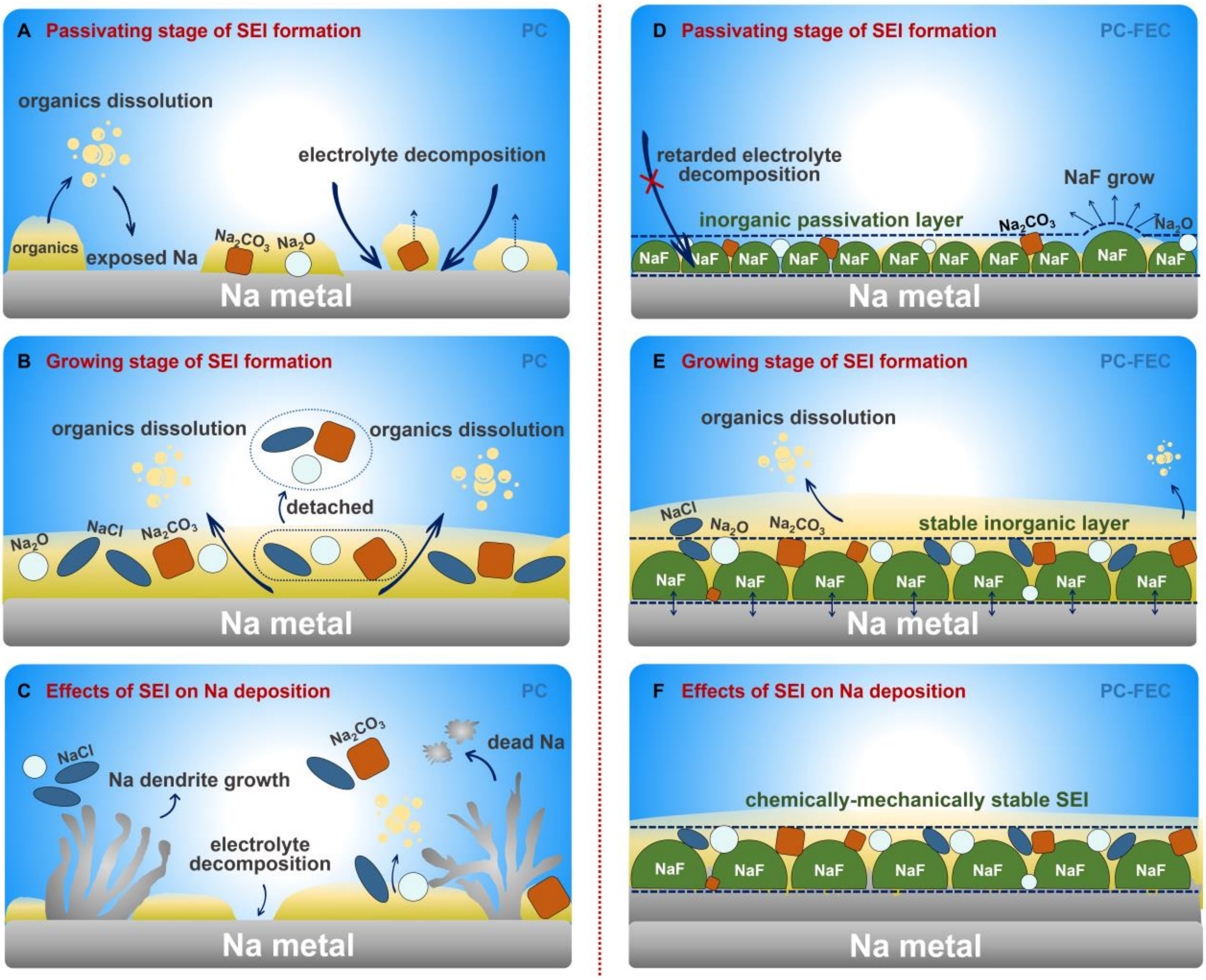

Scheme 1. Schematic illustration of SEI formation

(A-C) SEI formation process at different stages in PC.

(D-F) SEI formation process at different stages in PC-FEC.